ACS APPLIED MATERIALS & INTERFACES

Research Article

www.acsami.org

# $TiO_2$ Nanotube Array—Graphene—CdS Quantum Dots Composite Film in Z-Scheme with Enhanced Photoactivity and Photostability

Jiangjun Xian, Danzhen Li,* Jing Chen, Xiaofang Li, Miao He, Yu Shao, Linhui Yu, and Jialin Fang

Research Institute of Photocatalysis, State Key Laboratory of Photocatalysis on Energy and Environment, Fuzhou University, Fuzhou 350002, P. R. China

Supporting Information

**ABSTRACT:** The most efficient solar energy utilization is achieved in natural photosynthesis through elaborate cell membrane with many types of molecules ingeniously transferring photogenerated electrons to reactants in a manner similar to the so-called Z-scheme mechanism. However, artificial photosynthetic systems based on semiconductor nanoparticles are inevitably accompanied by undesired non-Z-scheme electron transfer and back reactions, which adversely affect the photoactivity and photostability of the systems. Herein, we report on a novel Z-scheme system with an electrochemically converted graphene (GR) film as the electron mediator interlayer contacted with both $TiO_2$ nanotube (TNT) array and CdS quantum dots (CdS QDs) on two sides. The obtained $TiO_2$ nanotube array—graphene—CdS quantum dots (TNT-GR-CdS) composite film shows higher photoelectric response and photocatalytic activities than other bare TNT, TNT-CdS, TNT-GR, and TNT-CdS-GR. Moreover, compared to TNT-CdS, the activity stability is significantly improved, and the residual amount of Cd element in reaction solution is reduced ~8 times over TNT-GR-CdS. Various measurements of photoelectrochemistry and radicals reveal that the enhanced photoactivity and photostabilities of TNT-GR-CdS are due to the efficient spatial separation of the photogenerated electron—hole pairs and the restricted photocorrosion of CdS via an efficient Z-scheme mechanism under simulated sunlight.

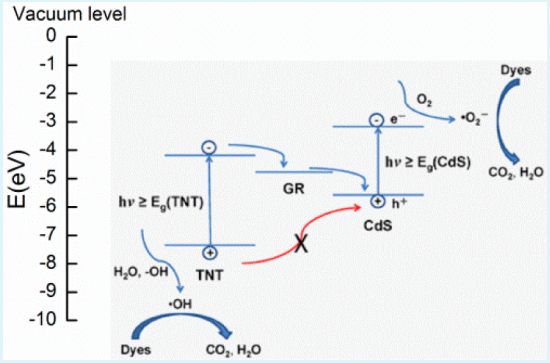


**KEYWORDS:** *nanotube, composite, Z-scheme, photoelectrochemistry, photocatalysis*

## INTRODUCTION

Semiconductor heterogeneous photocatalysis has received great attention for several decades as an effective pathway to solve the global energy crisis and environment deterioration.[1] Owing to high activity, good stability, nontoxicity, and low cost, $TiO_2$, as one of the most promising photocatalysts, has been widely used in photocatalytic purification of wastewater and air, hydrogen production, solar cells, and photoelectrochemical (PEC) devices.[1−3] However, $TiO_2$ is only responsive to a narrow ultraviolet (UV) light range (no more than 5% of total sunlight) due to intrinsic wide band gap, and the low quantum efficiency of $TiO_2$ photocatalysis is mainly because of high recombination of photogenerated electrons and holes, which limit its large-scale practical application.[4]

To break the bottleneck, various methods have been developed to expand the optical absorption range of $TiO_2$ and enhance the separation efficiency of photogenerated electron—hole pairs via doping,[5−7] modification,[8−10] or semiconductor coupling with forming heterojunction.[11−13] Notably, by using $TiO_2$ nanoparticle (TNP), an all-solid-state artificial photosynthesis system consisting of two photoexcitation systems and an electron mediator (e.g., $TiO_2$-Au-CdS),[14] often called the three-component (3C) Z-scheme system, has been demonstrated with much higher photocatalytic activity than single- and two-component (1C and 2C, respectively) systems. Most of the particulate Z-scheme systems were constructed by a noble metal core and a sensitizer shell locating on another semiconductor substrate.[15,16] Recently, graphene (GR) or reduced graphene oxide (RGO) was widely used to replace noble metal in a variety of nanocomposites[17,18] due to its high charge carrier mobility and large surface area.[19−22] The particulate Z-scheme systems consisting of GR as electron mediator and two nanoparticles (e.g., $BiVO_4$-RGO-Ru/$SrTiO_3$:Rh)[23] have shown greatly enhanced photocatalytic activity for completely splitting water under sunlight. However, all of these particulate systems involved disordered dispersion of particles and unclear composite structure, which led to adverse non-Z-scheme electron transfer and back reactions. For example, inevitable TNP-CdS contact in TNP-Au@CdS or TNP-GR-CdS would result in undesired transport of holes from TNP to CdS and increase the photocorrosion reactions of CdS, which adversely affect the photoactivity and photostability of the systems.

On the other hand, the vertically oriented $TiO_2$ nanotube (TNT) array prepared by electrochemical anodization of a Ti foil has larger specific surface area, faster charge transport, and

Received: May 15, 2014
Accepted: July 24, 2014
Published: July 24, 2014

  

better reusability than traditional TNP.[24,25] The successive combination of TNT array, GR film, and CdS quantum dots (QDs) could form a 3C composite film in Z-scheme (TNT-GR-CdS) with clear structure, in which the direct TNT-CdS contacts were separated by the GR interlayer. Thus, it may retard back reactions and increase the system efficiency. Furthermore, composite film system can avoid the drawbacks of particulate system including the agglomeration and the need of the high costs of the concomitant filtration facilities to recover the catalyst.[15] To the best of our knowledge, the construction of TNT-GR-CdS composite film in Z-scheme with efficiently improved photoactivity and photostability has not been studied so far.

Herein, it is reported for the first time to use the *in situ* electrochemically converted GR (ECG) film[26] coupling with TNT array and CdS QDs to fabricate a series of composite films, of which the clear composite structure can be easily controlled by changing the number and order of component layers. When GR film as the modulator interlayer of electron was contacted with both TNT and CdS, a novel TNT-GR-CdS composite film in Z-scheme was formed. The morphology, structure, crystal phase, and chemical composition of this film electrode were characterized in detail. By various measurements of PEC and photocatalytic activity, the 3C Z-scheme system showed higher PEC and photocatalytic properties than 1C (TNT), 2C (TNT-CdS, TNT-GR), and 3C non-Z-scheme (TNT-CdS-GR) systems. Moreover, compared to TNT-CdS, the efficiently improved photoactivity and photostability were also achieved in TNT-GR-CdS. The synergetic enhancement mechanism of the 3C Z-scheme composite film was discussed and proposed carefully.

## EXPERIMENTAL SECTION

**1. Preparation of Different TNT-Based Film Electrodes.** The highly ordered TNT films were prepared by electrochemically anodizing Ti foil (2 cm × 5 cm in size, 100 $\mu$m thick, 99.5% purity, General Research Institute for Nonferrous Metals, China) in a two-electrode electrochemical cell with a Ti foil as working anode and a graphite foil as counter cathode at room temperature. Before anodization, all Ti foils were orderly degreased in acetone, ethanol, and distilled water for 15 min by ultrasonication and were finally dried in air prior to use. The cleaned Ti foil was anodized in a 200 mL ethylene glycol (EG) solution containing 0.5 wt % $NH_4F$ and 2 vol % $H_2O$ (i.e., 4 mL of $H_2O$ and 196 mL of EG) at 20 V for 2 h. Then the TNT films were rinsed carefully by deionized water and annealed at 400 °C in air for 2 h with heating and cooling rate of 2 °C/min to obtain anatase crystalline phase.

Deposition of GR film on TNT or TNT-CdS electrode was carried out by a simple and green stabilized-voltage electrochemical reduction process. The graphene oxide (GO) solution was prepared from natural flake graphite by a modified Hummers method.[27,28] Then it was exfoliated completely by ultrasonication for 15 min as the electrolyte of reduction process. Typically, the TNT film electrode (cut into 1 cm × 5 cm in size) was immersed in a 50 mL exfoliated GO solution of 1 mg·mL$^{-1}$ concentration. The GR film was deposited on the TNT surface at 20 V for 30 min, and then the achieved TNT-GR composite film electrode was rinsed softly with deionized water and dried naturally in air prior to characterization. For comparing with TNT-GR, the TNT-GO sample was prepared when GO solution was directly dried on TNT film without the electrochemical reduction process.

CdS QDs were prepared on different TNT-based films by a successive ionic layer adsorption and reaction (SILAR) method.[29] Typically, the sample was successively immersed in four different beakers for ~30 s each time. One beaker contained 50 mmol·L$^{-1}$ $Cd(NO_3)_2$ aqueous solution, another contained 50 mmol·L$^{-1}$ $Na_2S$, and the other two contained distilled water to rinse the samples from the excess of each precursor solution. Such an immersion cycle was repeated several times, typically between 10 and 30 cycles. After several cycles the sample became dark yellow. Finally, the as-prepared samples were dried in a $N_2$ stream.

**2. Characterizations.** Field emission scanning electron microscopy (FESEM) images of the samples were examined using an instrument (S4800, Hitachi Co., Japan) operated at 20 kV. Transmission electron microscopy (TEM) images were detected by an instrument (Tecnai G2 F20, FEI Co., USA) operated at an accelerating voltage of 200 kV. The XRD patterns were recorded using an X-ray diffractometer (D8 Advance, Bruker Co., Germany) equipped with a film attachment under Ni-filtered Cu K$\alpha$ radiation. Measurements were carried out in $2\theta$ range from 10° to 80° at the scan rate of 0.02°/s. Raman spectra were recorded at room temperature using a confocal microscopy-Raman spectrometer (inVia, Renishaw Co., Britain) in the backscattering geometry with a 785 nm diode laser as an excitation source. The accelerating voltage and the applied current were 40 kV and 40 mA, respectively. The X-ray photoelectron spectroscopy (XPS) measurements were conducted on a photoelectron spectrometer (ESCALAB 250, Thermo Fisher Scientific Inc., USA) at 2.4 × 10$^{-10}$ mbar using a monochromatic Al K$\alpha$ X-ray beam (1486.6 eV). The binding energy of all elements was calibrated to the carbon binding energy of 284.5 eV. The UV−visible (UV−vis) diffuse reflectance spectra (DRS) were performed on a Varian Cary 500 spectrometer with an integrating sphere attachment ranging from 200 to 800 nm. And $BaSO_4$ was used as a reference sample in DRS measurements. The method of inductively coupled plasma-mass spectrometry (ICP-MS) was used to determine residue concentration of Cd ions in the reaction solution on an instrument (XSERIES 2, Thermo Fisher Scientific Inc., USA) at a frequency of 27.12 MHz. The 5,5-dimethyl-1-pyrroline-*N*-oxide (DMPO)-trapping electron spin resonance (ESR) technique was measured on a spectrometer (A300, Bruker Co., Germany) with the settings as follows: center field, 3512 G; microwave frequency, 9.86 GHz; microwave power, 20 mW.

**3. Measurements of Photoelectrochemistry.** All PEC measurements were performed on an electrochemical workstation (CHI 660D, Chenhua Instrument Co., China) in a standard three-electrode system using the as-prepared sample foils as the working electrodes (cut into 1 cm × 5 cm in size) with a light area of 0.5 cm × 0.5 cm = 0.25 cm$^2$, a Pt wire as the counter electrode, and a Ag/AgCl (saturated in KCl) as the reference electrode. The light source was a xenon arc lamp irradiation through a filter cutting off infrared light (marked as UV−vis, 320 nm < $\lambda$ < 800 nm) with an intensity of 265 mW/cm$^2$. The open circuit potential (OCP) versus time plots were recorded in 50 mmol·L$^{-1}$ $Na_2S$ electrolyte under intermittent UV−vis light irradiation with several on/off light cycles. Electrochemical impedance spectroscopy (EIS) tests of different samples were conducted in 10.0 mmol·L$^{-1}$ $Fe(CN)_6^{3-}/Fe(CN)_6^{4-}$ (1:1) mixture with 0.1 M KCl during dark. Linear sweep voltammetry (LSV) measurements were performed in 50 mmol·L$^{-1}$ $Na_2S$ electrolyte with potential scanning from 0.8 V to −0.6 V versus Ag/AgCl at the rate of 10 mV/s under the illumination of UV−vis light. The transient photocurrent versus time plots were measured in 100 mmol·L$^{-1}$ $Na_2SO_4$ electrolyte at bias of 0 V versus Ag/AgCl under the UV−vis illumination with on/off light cycles of 20 s intervals.

**4. Tests of Photocatalytic Activity.** The photocatalytic activity was evaluated by degradation of 10 $\mu$M rhodamine B (RhB) solution under the same UV−vis light irradiation as the PEC measurements. Typically, a piece of TNT-GR-CdS composite film electrode with active area about 1 cm × 3 cm = 3 cm$^2$ dipping into 3 mL of RhB solution in a quartz cuvette, which was 30 cm from the light source. Prior to irradiation, the sample foil was kept immersed in solution to adsorb RhB molecule in dark for 1 h to ensure the establishment of adsorption/desorption equilibrium, and then the light was turned on to degrade RhB. After a specific time interval (20 min for dark and 30 min for light), the concentration change of RhB solution was determined from the maximum absorption ($\lambda$ = 554 nm) measurements by a Varian Cary 50 Scan UV−vis spectrophotometer. The photocatalytic degradation efficiency was described by the concentration ratio $C/C_0$ after and before a certain reaction time. The whole

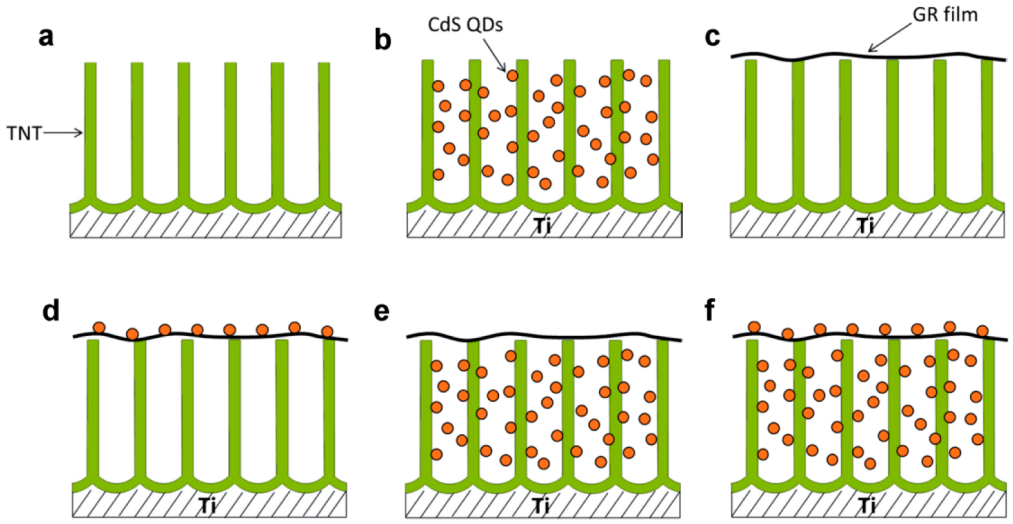


**Figure 1.** Design and architectures of (a) the original TNT electrode, (b) the TNT-CdS QDs, (c) the TNT-GR, (d) the TNT-GR-CdS, (e) the TNT-CdS-GR, and (f) the TNT-CdS-GR-CdS composite film electrodes.

process of photocatalytic degradation of RhB can be depicted by pseudo-first-order kinetics equation: $\ln(C_0/C) = k \times t$, where $k$ is the photocatalytic reaction apparent rate constant, $t$ is the reaction time, $C$ is the real maximum absorbance of RhB at time $t$, and $C_0$ in the equation is the absorbance at 554 nm when the dark adsorption equilibrium was achieved. To describe the photocatalytic activity more reasonably, the comparison of the $k$ value between different TNT-based composite films was demonstrated by the relation of $\ln(C_0/C)$ to $t$.

## RESULTS AND DISCUSSION

**Design and Architecture.** The design and architectures of different TNT-based composite films are schematically shown in Figure 1. The original ordered TNT array electrode was obtained (Figure 1a) via an electrochemical anodization of a Ti foil.[30] By using a SILAR method,[29] some CdS QDs were introduced into the inside of a TNT electrode to produce TNT-CdS (Figure 1b). A piece of GR film was directly deposited on the surface of a TNT electrode to form TNT-GR (Figure 1c) via a controllable one-step electrochemical reduction of GO solution at ambient conditions.[26] The 3C composite films consisting of TNT array, GR film, and CdS QDs with different orders could be fabricated by using the two modification methods alternately. TNT-GR-CdS in Z-scheme (Figure 1d) was produced when TNT combined with GR before with CdS QDs; thus, the GR could be as the mediator between TNT and CdS. While TNT-CdS-GR in non-Z-scheme (Figure 1e) was formed when combining TNT with CdS before with GR, TNT-CdS-GR-CdS (Figure 1f) was obtained by further combining TNT-CdS-GR with CdS QDs. In fact, TNT-GR-CdS and TNT-CdS-GR-CdS showed similar composite structure due to the small role of inner CdS covered by GR film. Therefore, the study was focused on the synergetic enhancement effect of TNT-GR-CdS in the Z-scheme, while the characterization of TNT-CdS-GR-CdS was ignored considering that its preparation process was the most tedious.

**Morphology and Structure.** Surface morphologies of the different composite films were characterized by FESEM. Figure 2a shows the nanotube-array structure of bare TNT film. After the electrochemical reduction of GO solution, TNT-GR presents a thin GR film depositing on the TNT surface with some wrinkles in Figure 2b. Moreover, the nanotube structure

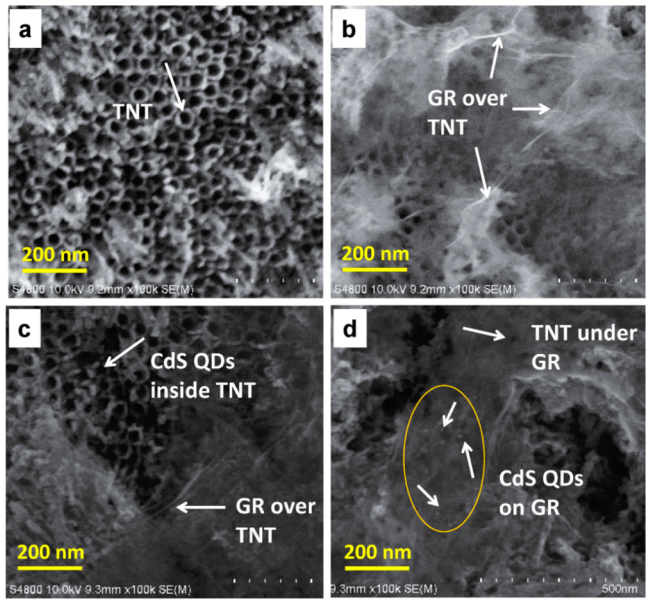


**Figure 2.** FESEM images of (a) the bare TNT electrode, (b) the TNT-GR, (c) the TNT-CdS-GR, and (d) the TNT-GR-CdS composite film electrodes.

is still clear under the GR film, demonstrating high transmittance. For TNT-CdS-GR, Figure 2c shows that CdS QDs are only located on the mouth and inner wall of the nanotubes, and the top surface of TNT is covered by GR film, which is in accord with its non-Z-scheme architecture. For TNT-GR-CdS, Figure 2d reveals that TNT is covered by GR film and that CdS QDs are dispersed evenly on the GR film, which was therefore contacted both with TNT and CdS QDs to form a Z-scheme.

The geometrical structure of TNT-GR-CdS composite film was further characterized by TEM. As shown in Figure 3a,b, the nanotube array structure of TNT is transformed into the pore array framework because of a scraping method used in TEM measurement. The edge of GR film is clear in these figures, and the CdS QDs are evenly dispersed on the film but not located on the nanotube wall of TNT, which is consistent with the Z-scheme structure of TNT-GR-CdS. The high-resolution transmission electron microscopy (HRTEM) images (Figure

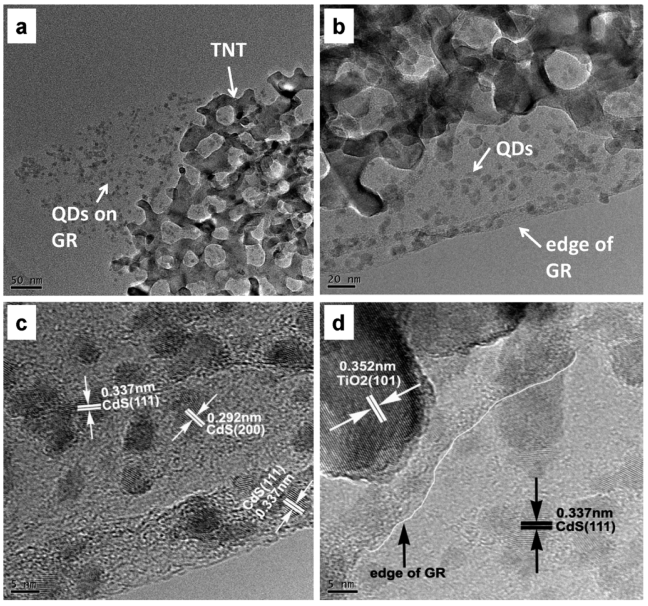


**Figure 3.** (a, b) The low-magnification TEM images and (c, d) the HRTEM images of the TNT-GR-CdS composite film scraped in ethanol dispersion solution.

3c,d) reveal that the average size of the nanoparticles on GR film is about 5 nm and that their lattice spacing corresponds to CdS crystal phase demonstrating the existence of CdS QDs. Moreover, the lattice spacing of the pore array framework is assigned to the anatase phase of $TiO_2$, proving the presence of TNT. These FESEM and TEM images are consistent with the design and architectures as shown in Figure 1, which indicates that the various composite films are fabricated in a controllable way.

**Crystal Phase and Chemical Composition.** In the XRD pattern of TNT-GR-CdS composite film (Supporting Information, Figure S1), all of the diffraction peaks are ascribed to anatase-phase $TiO_2$ and Ti substrate. The absence of GR peak can be attributed to the thinness of the GR film and/or to the close XRD peak positions of anatase TNT (101) and GR (002) located around 26° $2\theta$.[31] No obvious CdS peak may be due to the high dispersion and quantum size effect of CdS QDs. To further evidence the phase composition, Raman spectra of different composite films are characterized. As can be seen in Figure 4, TNT shows four peaks corresponding to 144, 398, 515, and 640 $cm^{-1}$, which are assigned as anatase-phase $TiO_2$, further demonstrating the existence of TNT phase. There is no obvious characteristic peak of CdS phase in the Raman spectra of TNT-CdS, TNT-CdS-GR, and TNT-GR-CdS, which may also be attributed to the high dispersion and quantum size effect of CdS QDs. However, the presence of CdS can be proved in the foregoing TEM and the latter XPS measurements. In addition, the D band (~1308 $cm^{-1}$) and G band (~1596 $cm^{-1}$) are observed in TNT-GR, TNT-CdS-GR, and TNT-GR-CdS, which belong to the characteristic peaks of graphitized structures confirming the presence of GR phase. The position of D band is little lower than the value of reference literature (~1354 $cm^{-1}$), which may be because of the interaction between TNT and GR film. The D/G intensity ratio bigger than one indicates the reduction of GO and the creation of many new smaller GR domains in the electrochemical reduction process.[32]

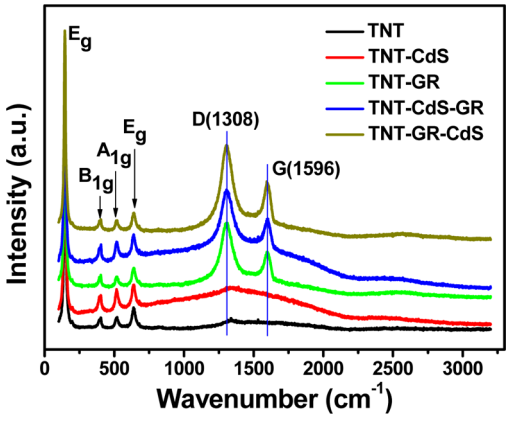


**Figure 4.** Raman spectra of the as-prepared different film electrodes.

To deeply characterize the chemical composition, XPS measurement of TNT-GR-CdS composite film was carried out. As shown in Figure 5a, the XPS survey reveals that the main composition elements of TNT-GR-CdS are Ti, O, Cd, C, S, and their atom contents (atom %) are shown in Supporting Information, Table S1. The molar ratio between Ti and O is 14.46:43.87, less than 1:2 because some additional O atoms exist in GR due to incomplete reduction of GO and exist in adsorbed oxygen on the surface, but most O atoms exist in $TiO_2$. The molar ratio between Cd and S is 2.76:2.94 ≈ 1:1, which is in line with the stoichiometric ratio of CdS. The C 1s spectrum of TNT-GO (Figure 5c) exhibits four peaks located at 284.5, 286.5, 287.5, and 288.6 eV corresponding to C−C, C−O, C═O, and O═C−OH, respectively. After electrochemical reduction, for TNT-GR-CdS (Figure 5b), the last three oxidized groups are slightly shifted to lower bonding energies due to incomplete reduction of these oxidized groups. Moreover, the O-bound C contents (Supporting Information, Table S3) of TNT-GR-CdS decreases drastically relative to that of TNT-GO (33.95% vs 64.23%) as expected. These data demonstrate that GO is efficiently reduced into GR in composite films via the electrochemical reduction process. Combing FESEM, TEM, Raman, and XPS characterizations, we can definitely suggest that TNT-GR-CdS is indeed the composite film of TNT, GR, and CdS QDs three phases.

**Optical Absorption.** Figure 6 presents the UV−vis diffuse reflection absorption spectra (DRS) of different film electrodes. As shown, bare TNT (black line) mainly absorbs the UV light below 380 nm depending on its intrinsic band gap. The weak visible-light absorption platform of bare TNT may be due to formation of surface state during the anodization process.[33] TNT-GR (green line) shows negligible improvement of visible-light absorption, indicating little contribution of GR to the visible-light excitation. The absorption edge of TNT-CdS (red line) exhibits an obvious red shift compared to bare TNT, and the whole absorption range is expanded to the visible region due to CdS QDs sensitization. TNT-CdS-GR (blue line) shows a little decrease of visible-light absorption compared to TNT-CdS (red line) because of the optical blocking effect of GR film over TNT-CdS. While coupling TNT with GR is before coupling with CdS QDs, these QDs highly dispersed on GR film can efficiently absorb the visible light. Thus, TNT-GR-CdS (dark yellow line) shows the best optical absorption among these composite films. In addition, as shown in Supporting Information, Figure S2, the band gap energy ($E_g$) of bare TNT is ~3.153 eV, and that of bulk CdS powder is ~2.25 eV.

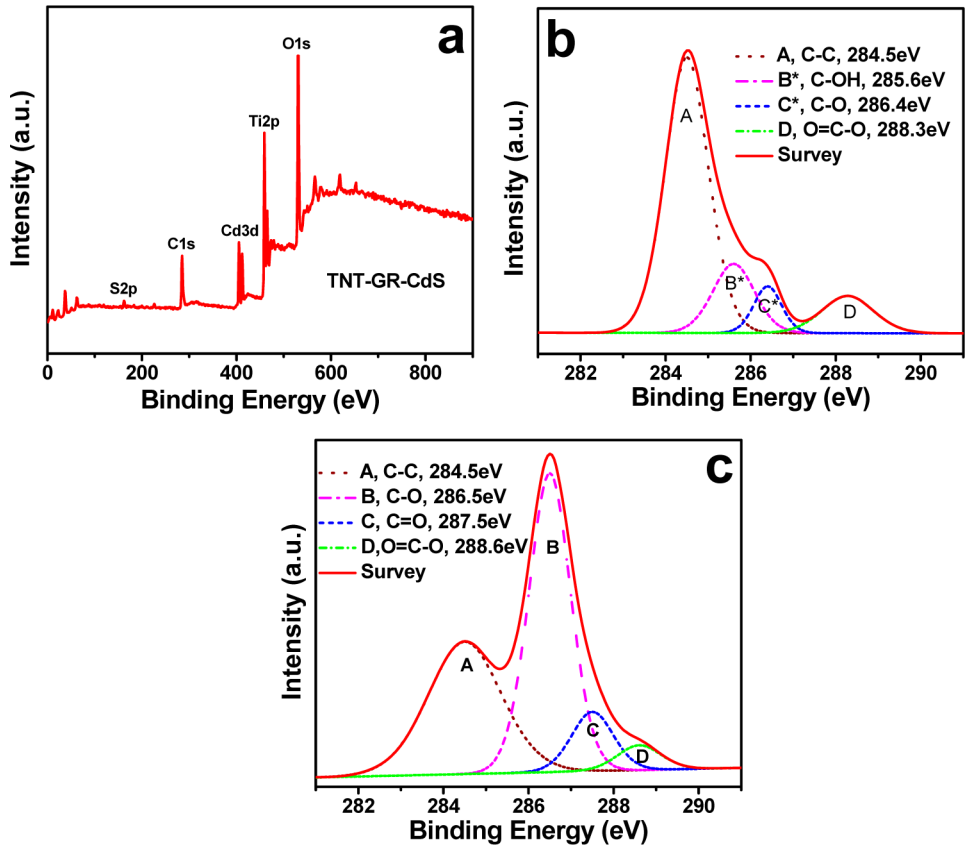


**Figure 5.** (a) The XPS survey of the TNT-GR-CdS composite film. The C 1s spectra of (b) the TNT-GR-CdS and (c) the TNT-GO composite films.

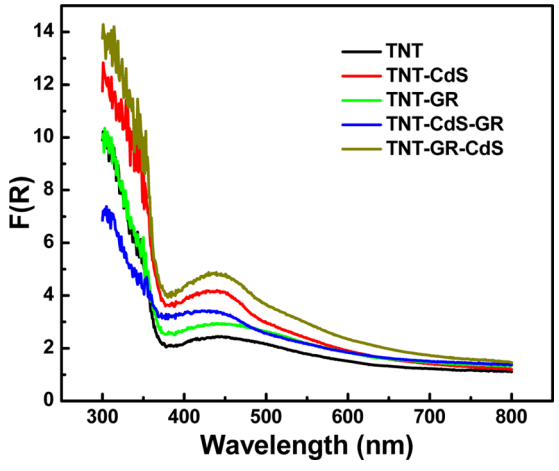


**Figure 6.** DRS spectra of the different film electrodes.

Although it was difficult to distinguish the exact absorption edge of the CdS QDs from the DRS spectra of the composite films, the quantum size of the CdS was proved in TEM measurements. Compared to bare TNT and the bulk CdS (Supporting Information, Figure S2a), the light absorption range of the TNT-GR-CdS composite film was expanded to a wider sunlight region because of the coupling of TNT, GR, and CdS QDs, which lays the good foundation for enhancing PEC and photocatalytic properties.

**Photoelectrochemical Properties.** To detailedly characterize the photoelectrochemical (PEC) properties of different sample electrodes, various electrochemical measurements were performed in a three-electrode system. The linear sweep voltammetry (LSV) measurements of different film electrodes under simulated sunlight irradiation are shown in Figure 7a. In a wide potential range from −0.4 to 0.8 V versus Ag/AgCl, TNT-GR-CdS shows the highest photocurrent density ($j_{ph}$) among all of the electrodes, indicating that it has greatly improved PEC performance. The detailed $j_{ph}$ values of different electrodes at bias of 0.6 V versus Ag/AgCl are shown in Supporting Information, Table S2. Compared to plain TNT, the $j_{ph}$ of TNT-CdS, TNT-GR, and TNT-CdS-GR are increased about 58%, 16.6%, and 8.66%, respectively; these enhancements probably result from the expanded light absorption and the multiple exciton generation of CdS QDs[34] as well as the increase of the charge-separation efficiency due to formation of heterojunction. The increments of TNT-GR and TNT-CdS-GR are lower than those of TNT-CdS, which can be ascribed to the blocking effect of GR film over TNT and TNT-CdS. While the $j_{ph}$ of TNT-GR-CdS is about 204% higher than that of TNT, that increment exceeds the sum of the increments with alone modification of CdS and GR. This synergetic enhancement infers that photogenerated electrons can more efficiently transfer from the 3C Z-scheme than they can from the 1C, 2C, and 3C non-Z-schemes to the counter electrode via external circuit.[35] Moreover, the transient photocurrent versus time measurements (Figure 7b) under an on/off cycle of simulated sunlight irradiation also show that the transient photocurrent of TNT-GR-CdS far exceeds that of the other electrodes and quickly achieves a stable $j_{ph}$ during light on. These results indicate that TNT-GR-CdS in 3C Z-scheme


dx.doi.org/10.1021/am5029999 | ACS Appl. Mater. Interfaces 2014, 6, 13157−13166

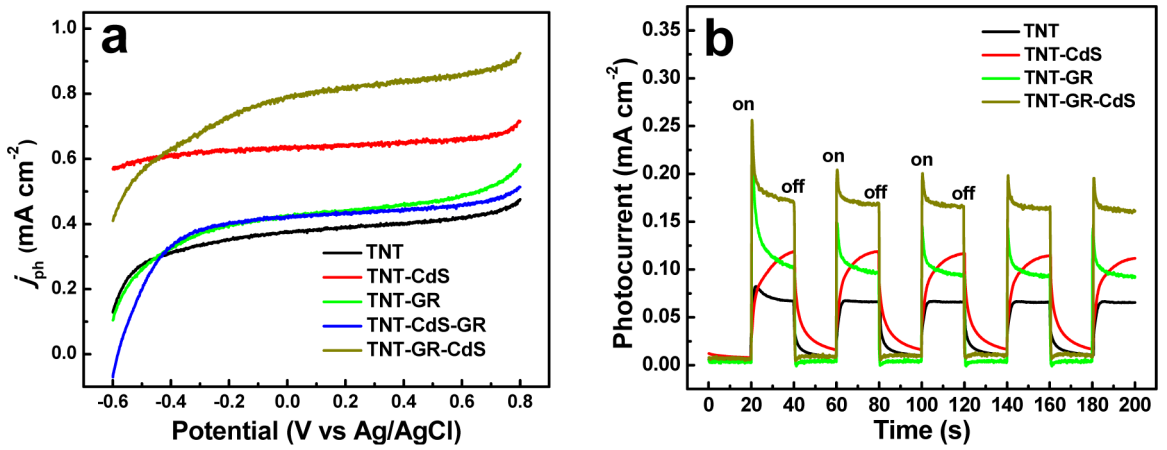


**Figure 7.** (a) The LSV tests in 50 mmol·L$^{-1}$ $Na_2S$ electrolyte and (b) the transient photocurrent responses vs time in 100 mmol·L$^{-1}$ $Na_2SO_4$ electrolyte at bias of 0 V vs Ag/AgCl with light on/off cycles for the different film electrodes under simulated solar light irradiation.

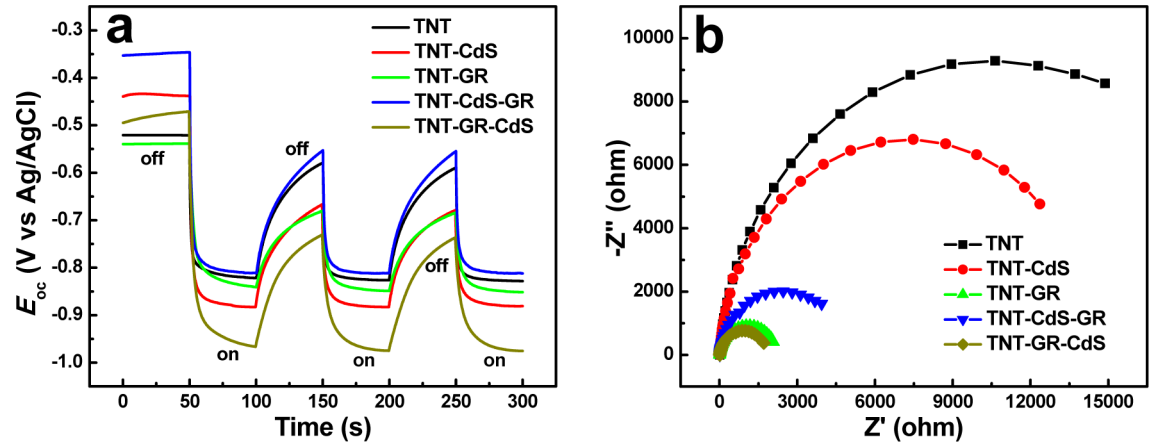


**Figure 8.** (a) The transient $E_{oc}$ responses in 50 mmol·L$^{-1}$ $Na_2S$ electrolyte with light on/off cycles under the simulated solar light irradiation and (b) the Nyquist plots of the EIS data measured in 10.0 mmol·L$^{-1}$ $Fe(CN)_6^{3-}/Fe(CN)_6^{4-}$ (1:1) mixture with 0.1 M KCl during dark for the different film electrodes.

significantly enhances the photoelectric response compared with 1C and 2C systems.

Figure 8a shows the transient open circuit potential ($E_{oc}$) of different film electrodes under intermittent simulated sunlight irradiation. Here, the much more negative photogenerated potential of TNT-GR-CdS (−0.9655 V vs Ag/AgCl) than the other electrodes indicates that electron energy in the 3C Z-scheme is promoted to a higher level than 1C, 2C, or 3C non-Z-scheme systems can provide by absorbing simulated sunlight. This phenomenon could be because the efficient charge separation in the Z-scheme makes the excitation of photoelectrons in TNT-GR-CdS at energy levels closer to the conduction band of CdS QDs than in all other cases,[36] which may be shifted to highly negative potential because of quantum size effect.[14] The corresponding photovoltage values are shown in Supporting Information, Figure S3. The photovoltage of TNT-GR-CdS is the highest among all of the sample electrodes, about 1.65 times higher than that of bare TNT due to the reasonable introduction of GR and CdS QDs, which indicates that the driving force of photogenerated charges in 3C Z-scheme was significantly enhanced. In addition, upon turning off the light, the $E_{oc}$ of TNT-GR-CdS decays more slowly than that of other electrodes, demonstrating the slower charge combination, that is, better separation efficiency of the photogenerated carriers in 3C Z-scheme composite film.

Electrochemical impedance spectroscopy (EIS) is a powerful tool for studying a material's electrochemical conductivity properties. The EIS measurement was carried out in the frequency range of $10^5$−0.1 Hz with amplitude of 5 mV at a bias potential of 0 V versus Ag/AgCl. It is known that the semicircle at high frequency in a Nyquist plot corresponds to the charge transfer limiting process and that the diameter of the semicircle is equal to the charge transfer resistance ($R_{ct}$). As can be seen in Figure 8b, TNT-GR, TNT-CdS-GR, and TNT-GR-CdS show much lower $R_{ct}$ than bare TNT and TNT-CdS, which is presumably owing to the introduction of the conductive GR layer. Notably, TNT-GR-CdS shows the smallest $R_{ct}$ value, even lower than that of TNT-GR and TNT-CdS-GR, implying the overall charge transfer is further improved when GR film is held between TNT array and CdS QDs in a Z-scheme, which is consistent with its good photoelectric response. Therefore, all of the PEC measurements clearly indicate that TNT-GR-CdS composite electrode exhibits much more efficient generation, separation, and transport of photogenerated carriers than 1C (TNT), 2C (TNT-CdS, TNT-GR), and 3C non-Z-scheme (TNT-CdS-GR) electrodes, which could result in significantly enhanced PEC and photocatalytic performances due to the synergetic effect of ordered TNT array, large-area GR interlayer, and evenly dispersed CdS QDs holding in a Z-scheme architecture.


dx.doi.org/10.1021/am5029999 | ACS Appl. Mater. Interfaces 2014, 6, 13157−13166

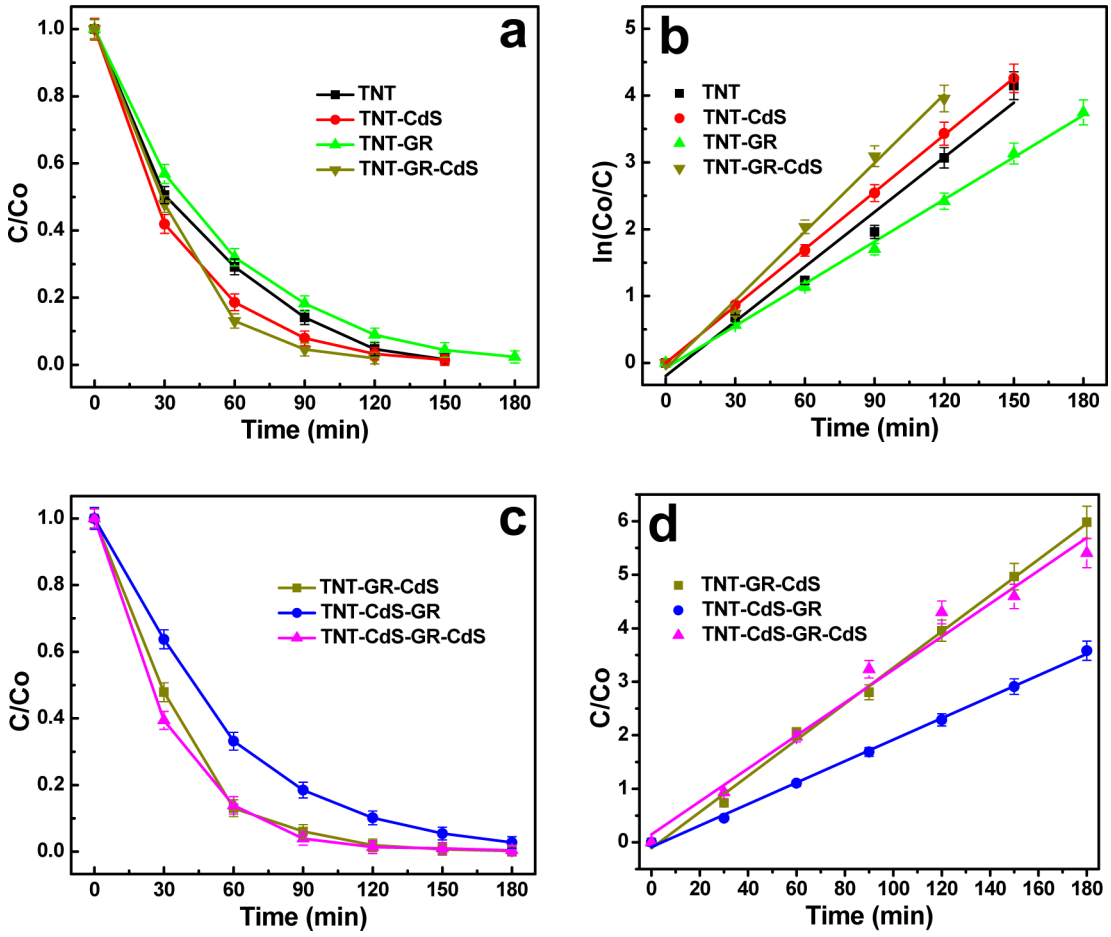


**Figure 9.** (a, c) The photocatalytic activities and (b, d) the linear fittings of the pseudo-first-order kinetics model in degrading the $1 \times 10^{-5}$ mol·L$^{-1}$ rhodamine B (RhB) solution over (a, b) the TNT-based films with different modification layers and (c, d) the ternary composite films with different structure orders under simulated solar light irradiation.

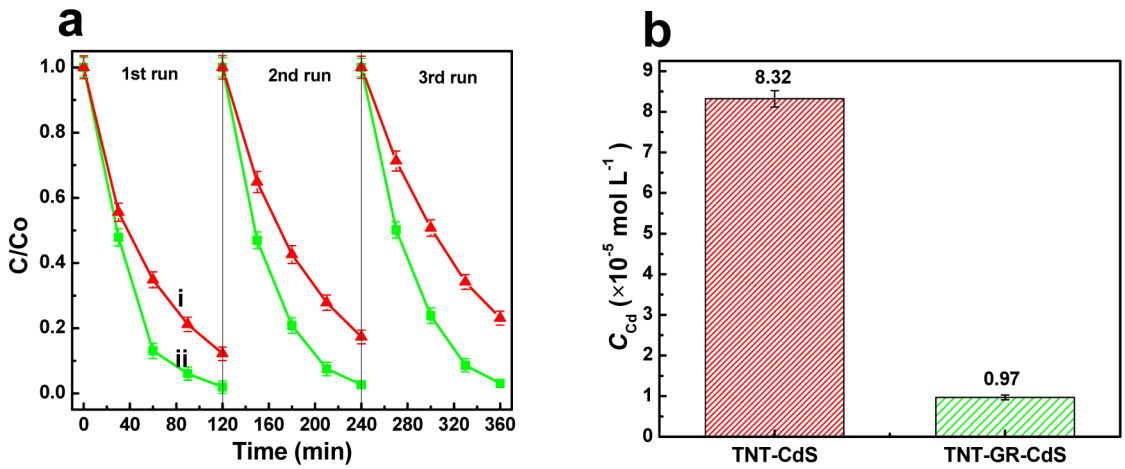


**Figure 10.** (a) The photocatalytic activity stability and (b) the residue concentration of Cd element in the reaction solution after degrading the $1 \times 10^{-5}$ mol·L$^{-1}$ RhB solution over (i) the TNT-CdS and (ii) the TNT-GR-CdS composite films under the simulated solar light irradiation.

**Photocatalytic Activities.** To further study the effects of composite structures on the photocatalytic activity, different sample films were estimated for degradation of rhodamine B (RhB) solution under simulated sunlight irradiation. Before turning on light (Supporting Information, Figure S4), TNT-GR-CdS composite film shows higher dye adsorption amount than 1C and 2C films due to the large surface area of GR and CdS QDs; this will be beneficial to the photocatalytic reaction. Figure 9a,b presents the effect of GR and/or CdS QDs on the photocatalytic activity. In Figure 9a, TNT-CdS (red line) shows higher photocatalytic degradation efficiency than bare TNT (black line), which could arise from the increase of the charge separation efficiency due to electron transfer from CdS to TNT, while TNT-GR (green line) decreases a little of the


dx.doi.org/10.1021/am5029999 | ACS Appl. Mater. Interfaces 2014, 6, 13157−13166

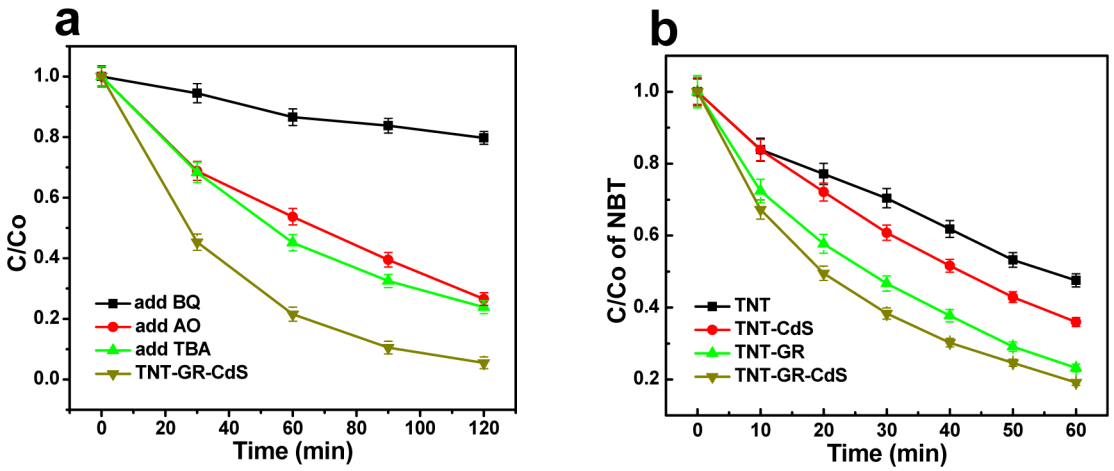


**Figure 11.** (a) The effect of the different radical scavengers on the photocatalytic degradation of RhB over the TNT-GR-CdS composite film and (b) the variation in the concentration of nitroblue tetrazolium (NBT) for tapping $^{\bullet}O_2^-$ over the different film electrodes under the simulated solar light irradiation. BQ: benzoquinone to trap $^{\bullet}O_2^-$, AO: ammonium oxalate to trap holes, TBA: *tert*-butyl alcohol to trap $^{\bullet}OH$.

photocatalytic activity compared to bare TNT, which should be due to the shield effect of GR film on the active sites of TNT. However, the photocatalytic activity of TNT-GR-CdS (dark yellow line) is higher than that of all bare TNT, TNT-CdS, and TNT-GR, which implies that combination of GR and CdS QDs can synergistically enhance the photocatalytic performance. The photocatalytic reaction rate described by linear fitting of quasi-first-order kinetics is exhibited in Figure 9b. The reaction rate constant of TNT-GR-CdS is still the highest among these films, further demonstrating the enhanced photocatalytic activity of 3C composite film compared with 1C and 2C systems.

Figure 9c,d shows the effect of different structure orders of 3C composite films on the photocatalytic activity. Clearly, the photocatalytic activities of TNT-GR-CdS and TNT-CdS-GR-CdS are very close, and they both are higher than that of TNT-CdS-GR. The similarity of activities of TNT-GR-CdS and TNT-CdS-GR-CdS can be ascribed to their similar composite structures due to the small role of inner CdS covered by GR film among the latter. The distinct slope difference of kinetics plots between TNT-GR-CdS and TNT-CdS-GR in Figure 9d further demonstrates that Z-scheme is more favorable than non-Z-scheme to enhance the photocatalytic activity of 3C composite film. Moreover, TNT-GR-CdS shows the higher activity stability (Figure 10a) than TNT-CdS, which demonstrates the improved photostability. On the other hand, the stable Raman spectra (Supporting Information, Figure S5a), XPS survey (Supporting Information, Figure S5b), and valence state of Cd element (Supporting Information, Figure S5c) also prove the chemical stability of TNT-GR-CdS in the photocatalytic process. In addition, the photocorrosion of CdS could release Cd ion in the solution, which is correlated with its photocorrosion degree. Especially, the residue concentration of Cd (Figure 10b) in the reaction solution using TNT-GR-CdS is significantly lower by ~8 times than that using TNT-CdS, which further explains the enhanced chemical stability and supports the improved photostability. These results demonstrate that 3C Z-scheme not only enhanced the photocatalytic activity but also greatly improved the photostability and chemical stability.

**Mechanism of the Enhancement of the Photocatalytic Performance.** Photocatalytic activity is closely related with the type and amount of the active species originated from photogenerated electron and holes. The radical trapping experiments (Figure 11a) reveal that the order of the radicals' effect is superoxide radical ($^{\bullet}O_2^-$) > hole ($h^+$) > hydroxyl radical ($^{\bullet}OH$) because of the shielding effect of GR film over the TNT inner layer. The DMPO-trapping ESR spectra (Supporting Information, Figure S6) show the $^{\bullet}OH$ intensities of TNT, TNT-CdS, and TNT-GR-CdS are almost the same and higher than those of TNT-CdS-GR and P25, which may be due to the destruction of composite structures in ESR measurement with scraping method. Moreover, the quantitative tests of the $^{\bullet}O_2^-$ (Figure 11b) indicate that the $^{\bullet}O_2^-$ amount of TNT-GR-CdS is apparently higher than that of other 1C and 2C samples. In addition, the detections of the $H_2O_2$ (Supporting Information, Figure S7) show the very small role of the $H_2O_2$ in the photocatalytic process. These results demonstrate that the $^{\bullet}O_2^-$ is the most important active species and that its amount is significantly increased over the 3C Z-scheme composite film.

To further interpret the enhancement effect, Scheme 1 shows the possible reaction mechanism on the basis of the energy-band diagram of the TNT-GR-CdS composite film. Plenty of studies have shown that the electron energy level of GR/$GR^{\bullet-}$ is slightly lower than the conduction band (CB) of anatase TNT,[37] which is lower than the CB of CdS.[14,15] On the basis of

**Scheme 1. Proposed Mechanism Diagram of the Enhancement of the Photocatalytic Activity over the TNT-GR-CdS Composite Film in Z-Scheme**

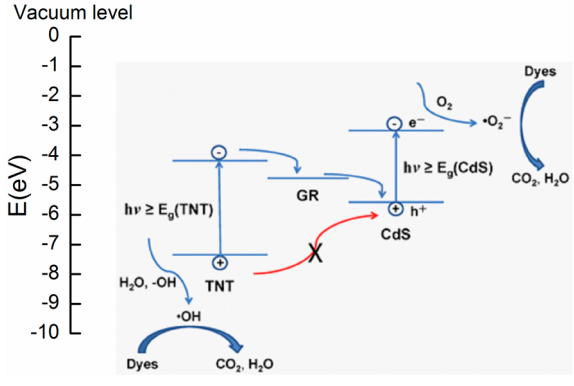



dx.doi.org/10.1021/am5029999 | ACS Appl. Mater. Interfaces 2014, 6, 13157−13166

DRS spectra (Figure 6) and band-gap energy (Supporting Information, Figure S2), upon irradiation with $h\nu \geq E_g$(CdS), the electrons are photoexcited from the valence band (VB) to the CB of CdS. Except for the recombination, the CB electrons of CdS have three ways of transferring: (1) to adsorbed $O_2$ on surface for generating superoxide radicals ($^{\bullet}O_2^-$); (2) to the CB of TNT substrate; (3) to carbon atoms of GR films. Since the majority of the CdS surfaces are occupied by adsorbed $O_2$ molecules, only small portions are in contact with GR film due to the CdS size quantization,[14,23] and the direct TNT-CdS contact is avoided by GR interlayer; thus, most of the CB electrons of CdS are consumed for photocatalytic reactions. The left VB holes of CdS inject to GR film (electron transfer I, GR → CdS), which is similar to the TNP-Au@CdS.[14]

Upon irradiation with $h\nu \geq E_g$(TNT), some part of the CB electrons of TNT can also reduce $O_2$ to participate in photocatalytic process due to its higher electron energy level than $O_2/^{\bullet}O_2^-$; another part of the electrons tends to flow into GR film (electron transfer II, TNT → GR) because of GR's effect as electron collector and transporter like in most literature.[19,23,37] The left VB holes of TNT with a strong oxidation power oxidize contaminant (dyes) or solvent ($H_2O$) and surface hydroxy (−OH) to produce the hydroxyl radicals ($^{\bullet}$OH) rather than transfer to the VB of CdS (red line) because of negligible TNT-CdS contact area due to the barrier effect of GR interlayer (for the same reason the back electron transfer from CdS to TNT is inhibited). Therefore, under simulated sunlight irradiation, excitation of both TNT and CdS should result in simultaneous electron transfer I and II, that is, vectorial electron transfer of TNT → GR → CdS.[14,36] This charge transport of Z-scheme not only achieves the efficient spatial separation of the CB electrons of CdS with a strong reduction power and the VB holes of TNT with a strong oxidation power, but also supplies the electrons from the CB of TNT to the VB of CdS via GR film to restrict the photocorrosion of CdS, which explains the high photoactivity and photostability of TNT-GR-CdS composite film.

## CONCLUSION

In conclusion, a novel 3C hybrid film system exhibiting remarkably enhanced PEC and photocatalytic performances in a wide spectral response range was successfully realized by coupling ordered TNT array, GR film, and CdS QDs via a simple and controllable fabrication process with alternately using the electrochemical reduction of GO and SILAR methods. This combination not only expands the optical absorption range and increases the adsorption capacity but also enables the synergistic operation of the three phases in a Z-scheme mechanism, facilitates the efficient separation of photogenerated electrons with a high potential to produce abundant $^{\bullet}O_2^-$, and prevents the photocorrosion of CdS. Consequently, this 3C Z-scheme system shows higher PEC and photocatalytic properties than other 1C, 2C, and 3C non-Z-scheme systems under simulated sunlight. This work may offer a new thought to prepare the high-performance multi-component composite film with clear structure for efficient solar energy utilization in PEC and photocatalysis areas.

## ASSOCIATED CONTENT

### Supporting Information

Absorption, ESR, Raman, and DRS spectra, XRD patterns, photovoltage comparison displayed in a bar graph, plot of $C/C_0$ versus time. This material is available free of charge via the Internet at http://pubs.acs.org.

## AUTHOR INFORMATION

### Corresponding Author

*E-mail: dzli@fzu.edu.cn. Phone & Fax: (+86)591-83779256.

### Notes

The authors declare no competing financial interest.

## ACKNOWLEDGMENTS

This work was financially supported by the National Natural Science Foundation of China (21173047, 21073036, and 21373049) and the National Basic Research Program of China (973 Program, 2013CB632405).

## REFERENCES

(1) Kubacka, A.; Fernandez-Garcia, M.; Colon, G. Advanced Nanoarchitectures for Solar Photocatalytic Applications. *Chem. Rev.* **2012**, *112*, 1555−614.

(2) Hoffmann, M. R.; Martin, S. T.; Choi, W.; Bahnemann, D. W. Environmental Applications of Semiconductor Photocatalysis. *Chem. Rev.* **1995**, *95*, 69−96.

(3) Chen, X.; Shen, S.; Guo, L.; Mao, S. S. Semiconductor-Based Photocatalytic Hydrogen Generation. *Chem. Rev.* **2010**, *110*, 6503−6570.

(4) Kumar, S. G.; Devi, L. G. Review on Modified $TiO_2$ Photocatalysis under UV/Visible Light: Selected Results and Related Mechanisms on Interfacial Charge Carrier Transfer Dynamics. *J. Phys. Chem. A* **2011**, *115*, 13211−13241.

(5) Asahi, R.; Morikawa, T.; Ohwaki, T.; Aoki, K.; Taga, Y. Visible-Light Photocatalysis in Nitrogen-Doped Titanium Oxides. *Science* **2001**, *293*, 269−271.

(6) Ghicov, A.; Macak, J. M.; Tsuchiya, H.; Kunze, J.; Haeublein, V.; Frey, L.; Schmuki, P. Ion Implantation and Annealing for an Efficient N-Doping of $TiO_2$ Nanotubes. *Nano Lett.* **2006**, *6*, 1080−1082.

(7) Fan, X. Y.; Zhang, Y. H.; Xiao, P.; Hu, F.; Zhang, H. Preparation of High-Orderly $TiO_2$ Nanotubes in Organic Solution and Characterization of C-Doped $TiO_2$. *Chin. J. Chem. Phys.* **2007**, *20*, 753−758.

(8) Lucky, R. A.; Charpentier, P. A. A One-Step Approach to the Synthesis of $ZrO_2$-Modified $TiO_2$ Nanotubes in Supercritical Carbon Dioxide. *Adv. Mater.* **2008**, *20*, 1755−1759.

(9) El Ruby Mohamed, A.; Rohani, S. Modified $TiO_2$ Nanotube Arrays (TNTAs): Progressive Strategies Towards Visible Light Responsive Photoanode, a Review. *Energy Environ. Sci.* **2011**, *4*, 1065−1086.

(10) Lin, C. J.; Lu, Y. T.; Hsieh, C. H.; Chien, S. H. Surface Modification of Highly Ordered $TiO_2$ Nanotube Arrays for Efficient Photoelectrocatalytic Water Splitting. *Appl. Phys. Lett.* **2009**, *94*, 3.

(11) Hou, Y.; Li, X. Y.; Zou, X. J.; Quan, X.; Chen, G. C. Photoeletrocatalytic Activity of a $Cu_2O$-Loaded Self-Organized Highly Oriented $TiO_2$ Nanotube Array Electrode for 4-Chlorophenol Degradation. *Environ. Sci. Technol.* **2009**, *43*, 858−863.

(12) Kang, Q.; Liu, S.; Yang, L.; Cai, Q.; Grimes, C. A. Fabrication of PbS Nanoparticle-Sensitized $TiO_2$ Nanotube Arrays and Their Photoelectrochemical Properties. *ACS Appl. Mater. Interfaces* **2011**, *3*, 746−749.

(13) Subarna Banerjee, S. K. M.; Das, Prajna P.; Misra, Mano Synthesis of Coupled Semiconductor by Filling 1D $TiO_2$ Nanotubes with CdS. *Chem. Mater.* **2008**, *20*, 6784−6791.

(14) Tada, H.; Mitsui, T.; Kiyonaga, T.; Akita, T.; Tanaka, K. All-Solid-State Z-Scheme in CdS-Au-$TiO_2$ Three-Component Nanojunction System. *Nat. Mater.* **2006**, *5*, 782−786.

(15) Zhu, H.; Yang, B.; Xu, J.; Fu, Z.; Wen, M.; Guo, T.; Fu, S.; Zuo, J.; Zhang, S. Construction of Z-scheme Type CdS−Au−$TiO_2$ Hollow Nanorod Arrays with Enhanced Photocatalytic Activity. *Appl. Catal., B* **2009**, *90*, 463−469.

(16) Xie, K.; Wu, Q.; Wang, Y.; Guo, W.; Wang, M.; Sun, L.; Lin, C. Electrochemical Construction of Z-scheme Type CdS−Ag−$TiO_2$ Nanotube Arrays with Enhanced Photocatalytic Activity. *Electrochem. Commun.* **2011**, *13*, 1469−1472.
(17) Zhang, J.; Yu, J.; Jaroniec, M.; Gong, J. R. Noble Metal-Free Reduced Graphene Oxide-$Zn_xCd_{1-x}S$ Nanocomposite with Enhanced Solar Photocatalytic $H_2$-Production Performance. *Nano Lett.* **2012**, *12*, 4584−4589.
(18) Xie, G.; Zhang, K.; Guo, B.; Liu, Q.; Fang, L.; Gong, J. R. Graphene-Based Materials for Hydrogen Generation from Light-Driven Water Splitting. *Adv. Mater.* **2013**, *25*, 3820−3839.
(19) Li, Q.; Guo, B. D.; Yu, J. G.; Ran, J. R.; Zhang, B. H.; Yan, H. J.; Gong, J. R. Highly Efficient Visible-Light-Driven Photocatalytic Hydrogen Production of CdS-Cluster-Decorated Graphene Nanosheets. *J. Am. Chem. Soc.* **2011**, *133*, 10878−10884.
(20) Kim, H.; Moon, G.; Monllor-Satoca, D.; Park, Y.; Choi, W. Solar Photoconversion Using Graphene/$TiO_2$ Composites: Nanographene Shell on $TiO_2$ Core Versus $TiO_2$ Nanoparticles on Graphene Sheet. *J. Phys. Chem. C* **2012**, *116*, 1535−1543.
(21) Zhu, M.; Chen, P.; Liu, M. Graphene Oxide Enwrapped Ag/AgX (X = Br, Cl) Nanocomposite as a Highly Efficient Visible-Light Plasmonic Photocatalyst. *ACS Nano* **2011**, *5*, 4529−4536.
(22) Ng, Y. H.; Iwase, A.; Kudo, A.; Amal, R. Reducing Graphene Oxide on a Visible-Light $BiVO_4$ Photocatalyst for an Enhanced Photoelectrochemical Water Splitting. *J. Phys. Chem. Lett.* **2010**, *1*, 2607−2612.
(23) Iwase, A.; Ng, Y. H.; Ishiguro, Y.; Kudo, A.; Amal, R. Reduced Graphene Oxide as a Solid-State Electron Mediator in Z-Scheme Photocatalytic Water Splitting under Visible Light. *J. Am. Chem. Soc.* **2011**, *133*, 11054−11057.
(24) Wang, D. A.; Yu, B.; Wang, C. W.; Zhou, F.; Liu, W. M. A Novel Protocol Toward Perfect Alignment of Anodized $TiO_2$ Nanotubes. *Adv. Mater.* **2009**, *21*, 1964−1967.
(25) Macak, J. M.; Tsuchiya, H.; Ghicov, A.; Yasuda, K.; Hahn, R.; Bauer, S.; Schmuki, P. $TiO_2$ Nanotubes: Self-Organized Electrochemical Formation, Properties and Applications. *Curr. Opin. Solid State Mater. Sci.* **2007**, *11*, 3−18.
(26) Xian, J.; Li, D.; Chen, J.; Li, X.; He, M.; Shao, Y.; Yu, L.; Fang, J. A Large-Area Smooth Graphene Film on A $TiO_2$ Nanotube Array via a One-step Electrochemical Process. *J. Mater. Chem. A* **2014**, *2*, 5187−5192.
(27) Hummers, W. S., Jr.; Offeman, R. E. Preparation of Graphitic Oxide. *J. Am. Chem. Soc.* **1958**, *80*, 1339−1339.
(28) Wang, H.; Robinson, J. T.; Li, X.; Dai, H. Solvothermal Reduction of Chemically Exfoliated Graphene Sheets. *J. Am. Chem. Soc.* **2009**, *131*, 9910−9911.
(29) Baker, D. R.; Kamat, P. V. Photosensitization of $TiO_2$ Nanostructures with CdS Quantum Dots: Particulate versus Tubular Support Architectures. *Adv. Funct. Mater.* **2009**, *19*, 805−811.
(30) Ye, M. D.; Xin, X. K.; Lin, C. J.; Lin, Z. Q. High Efficiency Dye-Sensitized Solar Cells Based on Hierarchically Structured Nanotubes. *Nano Lett.* **2011**, *11*, 3214−3220.
(31) Perera, S. D.; Mariano, R. G.; Vu, K.; Nour, N.; Seitz, O.; Chabal, Y.; Balkus, K. J. Hydrothermal Synthesis of Graphene-$TiO_2$ Nanotube Composites with Enhanced Photocatalytic Activity. *ACS Catal.* **2012**, *2*, 949−956.
(32) Guo, H. L.; Wang, X. F.; Qian, Q. Y.; Wang, F. B.; Xia, X. H. A Green Approach to the Synthesis of Graphene Nanosheets. *ACS Nano* **2009**, *3*, 2653−2659.
(33) Mor, G. K.; Varghese, O. K.; Paulose, M.; Shankar, K.; Grimes, C. A. A Review on Highly Ordered, Vertically Oriented $TiO_2$ Nanotube Arrays: Fabrication, Material Properties, and Solar Energy Applications. *Sol. Energy Mater. Sol. Cells* **2006**, *90*, 2011−2075.
(34) Sun, W. T.; Yu, Y.; Pan, H. Y.; Gao, X. F.; Chen, Q.; Peng, L. M. CdS Quantum Dots Sensitized $TiO_2$ Nanotube-Array Photoelectrodes. *J. Am. Chem. Soc.* **2008**, *130*, 1124−1125.
(35) Xie, G.; Zhang, K.; Fang, H.; Guo, B.; Wang, R.; Yan, H.; Fang, L.; Gong, J. R. A Photoelectrochemical Investigation on the Synergetic Effect between CdS and Reduced Graphene Oxide for Solar-Energy Conversion. *Chem.—Asian J.* **2013**, *8*, 2395−2400.
(36) Yang, H.; Kershaw, S. V.; Wang, Y.; Gong, X.; Kalytchuk, S.; Rogach, A. L.; Teoh, W. Y. Shuttling Photoelectrochemical Electron Transport in Tricomponent CdS/rGO/$TiO_2$ Nanocomposites. *J. Phys. Chem. C* **2013**, *117*, 20406−20414.
(37) Xiang, Q. J.; Yu, J. G.; Jaroniec, M. Synergetic Effect of $MoS_2$ and Graphene as Cocatalysts for Enhanced Photocatalytic $H_2$ Production Activity of $TiO_2$ Nanoparticles. *J. Am. Chem. Soc.* **2012**, 6575−6578.